

Pressure driven flow of superfluid ^4He through a nanopipe

Jeffrey Botimer* and Peter Taborek†

Department of Physics & Astronomy, University of California Irvine, Irvine, California 92697, USA

(Received 4 May 2016; published 14 September 2016)

Pressure driven flow of superfluid helium through single high-aspect-ratio glass nanopipes into a vacuum has been studied for a wide range of pressure drop (0–30 bars), reservoir temperature (0.8–2.5 K), pipe lengths (1–30 mm), and pipe radii (131 and 230 nm). As a function of pressure drop we observe two distinct flow regimes above and below a critical pressure drop P_c . For $P < P_c$, the critical velocity is approximately the Feynman critical velocity. As the pressure drop approaches P_c , there is a sudden transition to a new flow state with a critical velocity more than an order of magnitude higher. The position of the transition is explained by a simple model that accounts for the fountain pressure generated by evaporative cooling at the outlet of the nanopipe.

DOI: [10.1103/PhysRevFluids.1.054102](https://doi.org/10.1103/PhysRevFluids.1.054102)

I. INTRODUCTION

The flow of superfluid helium (He II) through channels has been a subject of great interest for decades [1–3]. At low flow velocities, superfluid will flow as an ideal dissipationless fluid, but as the flow velocity increases, quantized vorticity can be generated, which leads to dissipation and pressure gradients. Vorticity can be generated from the irrotational background superflow via thermal [4] or quantum [5] (intrinsic) nucleation or it can be generated from preexisting (extrinsic) pinned vortex lines. For either mechanism, there is a critical velocity above which vorticity is generated very rapidly, so stable flow takes place at or near the critical velocity. Much of what is known about these critical velocities comes from two types of experiments. The first type measures the flow rate as a function of pressure through either a capillary [6–8] or a single hole [9–11] using a capacitive level sensor. These experiments had a complex phenomenology and were difficult to interpret and attention turned to experiments that utilized vibratory motion of a diaphragm with a hole; early experiments used micron-sized holes [12–14], while more recent experiments use holes in the range of 100 nm [15]. This type of measurement detects the onset of dissipation due to individual vortices, but does not directly monitor either flow rate or pressure drops. Theoretical models that describe the formation and motion of vorticity are based on nucleation theory [2,9,16], two-fluid-flow models [17–19], and Biot-Savart dynamics of vortex motion [20–22]. A recent review [3] summarizes over 50 years of superfluid flow data.

In most previous experiments on the flow of superfluid, a capillary or orifice connects two reservoirs of nominally isothermal bulk fluid with pressure differences of a few mbars or less. Recently, several experiments have explored a more complex flow regime in which superfluid flows from a bulk liquid reservoir into a vacuum through a nanoscale channel [23–25]. The high flow impedance of these channels enables the investigation of flows over a wide range of pressure drop. The reservoir pressure in the experiments reported here span the range from the saturated vapor pressure to the solidification pressure. The evaporative cooling that takes place on the low-pressure side of the channel produces temperature gradients that can directly drive superflows. The combination of large temperature and pressure gradients can generate unusual flows in which the superfluid-normal transition occurs inside the channel. These types of flows are interesting strongly driven nonequilibrium systems and are also important in cryogenic engineering. Standard evaporative

*jbotimer@uci.edu

†ptaborek@uci.edu

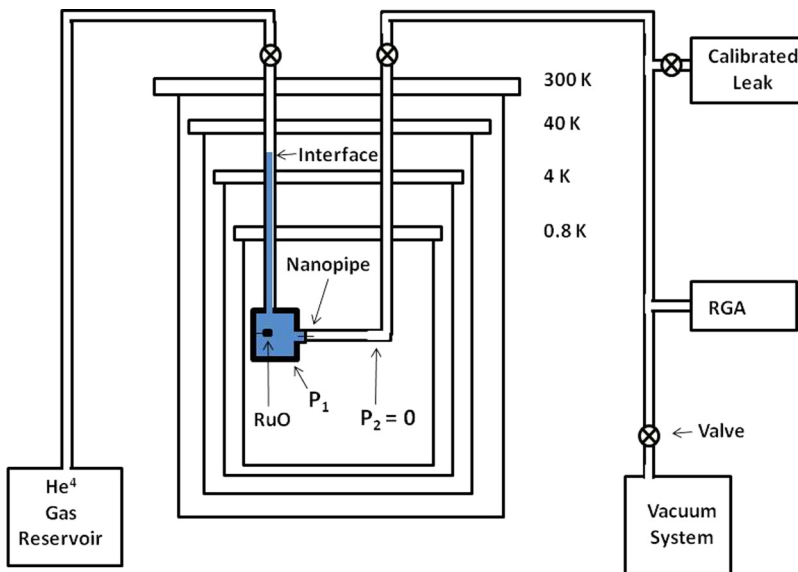


FIG. 1. Superfluid nanoflow experimental setup. The high-pressure reservoir is at temperature T_1 and pressure P_1 .

refrigerators utilize large pressure drops across micron and submicron capillaries in which liquid helium enters in the normal state and emerges in the superfluid state [26,27]. Similar flows occur in porous plug pumps and phase separators that are used in zero gravity [28,29].

In the work presented here we study the mass flow–pressure drop relation for superfluid helium flowing through single nanopipes with aspect ratios in the range of 10^4 – 10^5 for pressure drops ranging from 0 to 30 bars. The data show a large flow transition at a critical pressure drop that depends on the reservoir temperature.

II. EXPERIMENTAL APPARATUS AND METHODS

Figure 1 shows the experimental apparatus, which was composed of an input helium gas line, a copper pressure cell that served as a liquid reservoir, a glass nanopipe, and a vacuum pumping line. The flow apparatus was mounted in a continuous pulse tube ⁴He evaporation cryostat. The flow rate of helium through the nanopipe was measured using a Stanford Research Systems residual gas analyzer (RGA) running in continuous mode, a type of mass spectrometer. The RGA is a very sensitive detector of the partial pressure of helium in the pumping line. At the start of each experimental run, before helium was inserted into the cell, a background reading was obtained with the RGA and a calibrated helium leak was used to obtain a conversion between the partial pressure of helium and the helium mass flow. The RGA background was at least two orders of magnitude lower than any signal obtained from flow through the nanopipes. Details about the use of a mass spectrometer to measure helium flow rates have been documented previously [23,30].

The fused silica pipes acquired from Polymicro Technologies had nominal inside diameters of 0.2 and 0.4 μm , an outside diameter of 125 μm , and a protective outer polymer coating. Each pipe came in 10-m spools, with the same nominal inside diameter on both ends of the pipe. We independently measured the inside diameter of our prepared pipes *in situ* using normal ⁴He flow measurements and postmeasurement using a FEI Magellan 400 XHR scanning electron microscope (SEM). Our measured diameters were slightly larger than the nominal values, but the flow and SEM measurements were consistent between each pipe and agreed to within 6 nm. Pipe 1, for example, had a measured $r = 131$ nm and an SEM measured radius of 134.5 nm. An SEM image of the pipe

TABLE I. Dimensions of the four nanopipes discussed in this work. Each pipe's maximum pressure drop ΔP and minimum temperature T are also listed for reference.

Pipe	Nominal r (nm)	Measured r from Eq. (1) (nm)	L (mm)	ΔP_{\max} (bars)	T_{\min} (K)
1	100	131.2(\pm 0.7)	2.0	26.8	0.83
2	100	131.7 (\pm 0.7)	30	23.7	0.85
3	200	230.0 (\pm 1.4)	1.5	31.3	0.86
4	200	231.2 (\pm 1.4)	32	23.3	0.87

entrance can be found in Ref. [31]. In this work we report on four pipes, the dimensions of which can be found in Table I along with the maximum pressure drop ΔP and minimum temperature T . Additional pipes of radius $r = 131$ nm were measured, with lengths spanning the intermediate regime between lengths $L = 1$ and 30 mm, and they all exhibited the same behavior discussed below.

The pipes were prepared by first breaking off a length of pipe longer than needed. The polymer coating was then slowly burned off in a propane flame, taking care to not melt or bend the silica pipe; this was necessary to ensure adhesion of the epoxy. The pipe was then either sealed in a 1/8-in. Swagelok VCR male-male adapter in the case of the longer pipes or sealed in a 1-mm-thick \times 5-mm-diameter copper disk with a small hole drilled in the center in the case of the short pipes, using Stycast 2850 FT epoxy. The short pipes were then attached directly to a small copper pressure cell using the Swagelok VCR fitting, while the copper disk holding the short pipe replaced the traditional metal gasket used in the Swagelok VCR seals. Just before mounting the pipes to the copper pressure cell, the pipes were cleaved at the desired length. By saving this step until the last possible moment, the chance of contaminants entering the pipe was minimized.

A ruthenium oxide (RuO) thermometer was mounted inside the copper cell and submerged in the liquid helium to measure the helium temperature. A thermometer was also mounted to the exterior of the copper cell for monitoring purposes. The temperature was controlled to within 0.6 mK. The volume of the cell was $\sim 10^{-6}$ m³.

A 1/16-in. copper fill line connected the cell to a mechanically actuated, superfluid tight valve at the 0.83 K plate. A 1/16-in. stainless steel fill line ran from the valve to the 4 K plate, where 1/4-in. piping connected to an external helium pressure system. All measurements presented here were done with the valve open and the pressure measured by either an Omega PX309 pressure transducer (higher pressure) or a MKS Instruments Baratron (low pressure) at room temperature.

The low-pressure side of the pipe was connected to a turbo pump through a 1/4-in. stainless steel pipe. Maintaining a high vacuum (< 0.5 μ bar) is critical for the RGA to operate properly. In some experiments the mass flow and therefore the pressure became too large for the RGA to measure, so for higher mass flows a MKS Instruments Series 345 Pirani gauge was used. The RGA and Pirani gauge's working ranges overlapped between 9 and 25 ng/s, allowing for the Pirani gauge to be calibrated to the RGA each run. This approach is validated by the measured radius of the two $r = 230$ nm pipes (pipes 3 and 4). As will be discussed in more detail below, the pipe radius can be determined from *in situ* measurements using normal liquid ⁴He. Pipe 4 could be measured exclusively using the RGA, while the much shorter pipe 3 achieved normal flow rates of ~ 45 ng/s and required both the RGA and Pirani working in conjunction to cover the entire range of flow.

It should be noted that the low-pressure side of the pipe never exceeded 0.7 μ bar, even for the highest measured flow rates. Therefore, for the range of input pressures measured here, the pressure on the downstream side of the pipe can be accurately approximated as $P_2 \approx 0$ and the pressure drop is effectively the same as the input pressure P_1 .

Before cooling down, the cell was flushed with helium gas at least three times. The cell was then pressurized to ~ 0.6 bar, while the vacuum line was held near vacuum while the cell cooled down. Both the input line and vacuum line were then sealed with room temperature valves while

the cryostat cooled down. Once cold, the cell and vacuum line were evacuated while held at 6 K. Ultrahigh purity ^4He gas from Airgas (99.999%) passes through sintered, stainless steel mesh filters with a $0.5\text{-}\mu\text{m}$ nominal pore size from Swagelok (F series filter) before entering and after exiting the cell. The filters were thermally anchored at 4 K. The filters provided further purification of the ultrahigh-purity ^4He from trace gases and prevented contaminants from entering the cell.

All experiments were performed with bulk liquid ^4He in the cell. At pressures at or near the saturated vapor pressure (SVP), the cell was able to reach the base temperature (0.83 K). For higher pressures, the cell and part of the fill line were filled with liquid. In this configuration an additional heat load was carried by the liquid ^4He in the fill line from the 4 K plate to the base 0.83 K plate, so the lowest obtainable stable temperature was ~ 1.1 K. Experiments were done by either stepping the temperature and holding the pressure drop constant or stepping the pressure drop and holding the temperature constant. In the case of the SVP temperature sweep, the pressure was allowed to move along the SVP curve.

The density and pressure of liquid helium in the reservoir were monitored with the use of an *in situ* quartz tuning fork [32,33]. A fork similar to that described in Ref. [34] was used to verify the solidification of helium at high pressures.

III. RESULTS AND DISCUSSION

A. Normal flow behavior

To ensure that our system was working properly we first measured the flow of normal liquid ^4He at 2.3 K. For laminar flow of a normal fluid through a pipe, the mass flow can be approximately described by the Poiseuille mass flow equation

$$Q_m = \frac{\pi\rho\Delta P}{8\eta L}r^4, \quad (1)$$

where ΔP is the pressure drop across the pipe, L is the length of the pipe, r is the pipe radius and ρ is the density, and η is the dynamic viscosity evaluated at the temperature and pressure of the reservoir.

Figure 2 compares the measured mass flow through pipe 1 at various pressure drops with the prediction of Eq. (1). The deviation from linearity in Fig. 2 is due to the pressure dependence of both ρ and η , obtained from thermodynamic data [35–37]. The uncertainties in Fig. 2 and all figures are smaller than the data points displayed and so the error bars are omitted. A least-squares fit of the data using Eq. (1) gives a radius of 131.2 nm (± 0.7 nm) with a 99% confidence interval. Equation (1) is strictly valid for an incompressible isothermal flow, so a more conservative error of $\delta r = \pm 3$ nm, which is the approximate error in the SEM measurement of the radius, is perhaps more appropriate. The radius obtained using Eq. (1) agreed with the SEM measurements to within δr . The qualitative results presented in this work do not, however, depend sensitively on the exact value of r .

B. Flow transition at critical pressure

Although the mass flow vs pressure drop of normal ^4He can be explained with an isothermal viscous flow model, the mass flow of He II proved to be considerably more complicated. Figure 3 shows a number of isotherms for flow through pipe 1. As the pressure drop is increased from SVP for each temperature, the mass flow goes through a substantial and sharp transition at a critical pressure drop P_c to a much higher flow rate. The transition is quite sharp at low temperatures and becomes broader near T_λ , but the flow rate is always much higher than the normal liquid flow rate ($T = 2.30$ K data in Fig. 3).

Figure 3 also shows that P_c systematically increases with increasing temperature. There are a number of ways one could define P_c , whether it be at the start of the transition, the point of maximum curvature, or the point of maximum slope, etc. Here we have chosen to define P_c at the start of the transition for reasons that will be discussed in detail shortly.

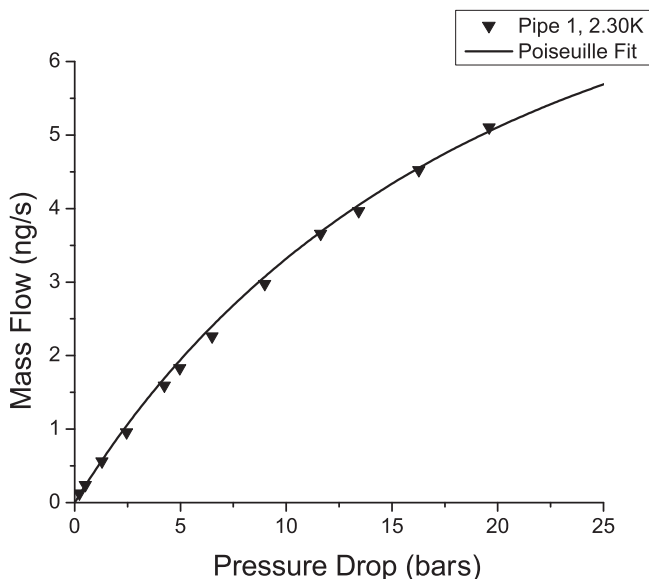


FIG. 2. Mass flow of normal ^4He through pipe 1 at 2.3 K as a function of the pressure drop. The solid line is the prediction of Eq. (1) for a pipe of radius 131 nm, assuming that the liquid density and viscosity in the nanopipe have the same values as in the high-pressure reservoir.

In addition to systematically increasing with temperature, P_c did not exhibit any observable hysteresis when the pressure drop was swept up and back down through the transition. This flow transition was observed in multiple pipes of varying lengths and radii. The location of P_c , at a given temperature, varies only slightly for pipes with lengths that vary by more than an order of magnitude, as shown in Fig. 4, but for each pipe the qualitative dependence on temperature is similar and lies in

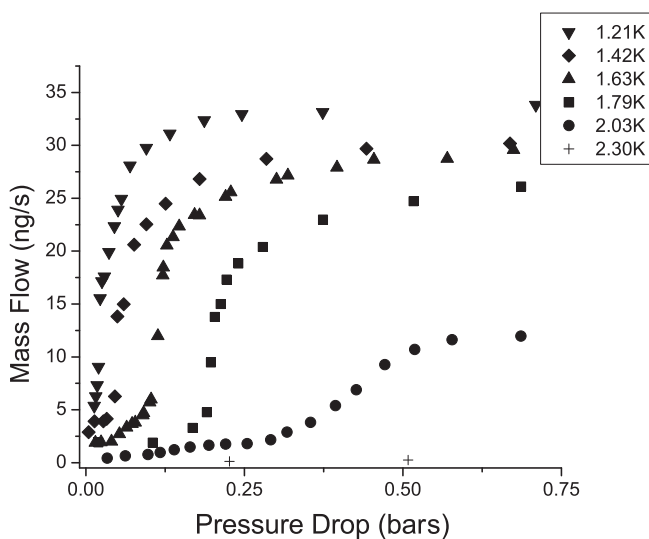


FIG. 3. Mass flow isotherms for various temperatures as a function of pressure drop through pipe 1 ($r = 131 \text{ nm} \times 2 \text{ mm}$): 1.21 K (▼), 1.42 K (◆), 1.63 K (▲), 1.79 K (■), 2.03 K (●), and 2.30 K (+). There is an abrupt increase in the mass flow at a critical pressure drop P_c that depends on temperature.

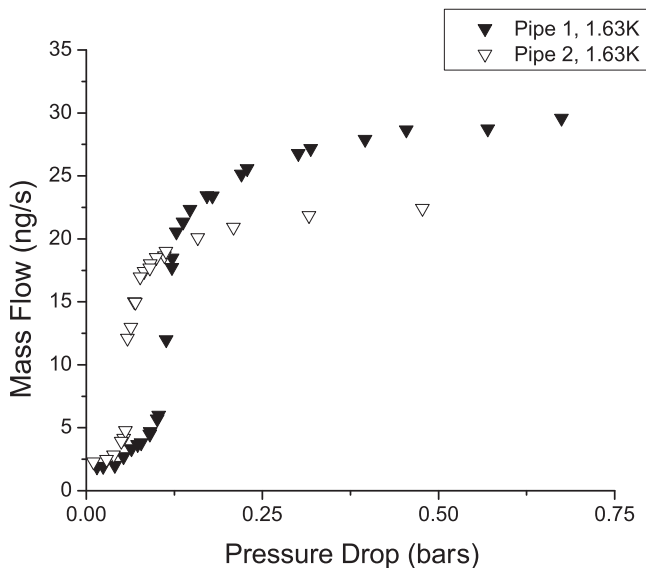


FIG. 4. Mass flow as a function of pressure drop through pipes of different length at 1.63 K: pipe 1 (closed triangles, $r = 131 \text{ nm} \times 2 \text{ mm}$) and pipe 2 (open triangles, $r = 131 \text{ nm} \times 30 \text{ mm}$). There is an abrupt increase in flow at a critical pressure drop P_c that varies only slightly for pipes with lengths that differ by more than an order of magnitude.

the 10–200 mbar range. The flow transition at P_c was observed in all of our pipes and P_c separated regimes of flow with distinctly different temperature and pressure drop dependence of the superfluid velocity, as will be discussed in more detail below.

A quantitative model for the flow requires an assumption on the state of the fluid at the low-pressure end of the pipe and in particular the position of the liquid-vapor interface. For the mass flows measured in our experiments, the liquid-vapor interface cannot occur inside the pipe in steady state because the mass transport of the vapor in the pipe is far too small [24]. For some combinations of pipe diameter and driving pressure, superfluid helium can emerge from the end of a pipe in a continuous stream like water coming out of a garden hose [38], but that is not possible in our apparatus. Generating a continuous stream or a stream of droplets requires the formation of a large amount of liquid-vapor interface. The energy to do this must come from the kinetic energy of the flow out of the nozzle. For liquid flowing out of a hole or pipe, there is a critical velocity v_{jet} at which the kinetic energy of the fluid can supply the surface energy for a continuous liquid jet to be formed. Below this critical velocity no jet can be formed and the liquid drips out of the pipe [39]. This critical velocity is

$$v_{\text{jet}} = 2\sqrt{\frac{\gamma}{\rho r}}, \quad (2)$$

where γ is the surface tension. Nanoscale pipes have a high surface to volume ratio, so the critical velocity can be quite high. For an $r = 130 \text{ nm}$ pipe, $v_{\text{jet}} \approx 8.4 \text{ m/s}$, which is higher than any velocity we observe. Thus, as the helium flows out of the low-pressure side of the pipe, the liquid will form a small pool around the low-pressure region of the pipe as shown in Fig. 5. The same type of analysis suggests that a pool of liquid will also form at the exit nozzle in several recent experiments involving flow into a vacuum [23,25].

Because the low-pressure side of the pipe is held at vacuum, the helium pool begins to evaporate with a mass flux density per unit time J_{evap} , which is determined by the pool

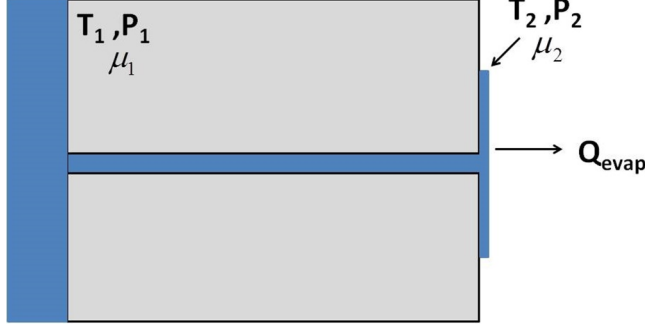


FIG. 5. Schematic of a nanopipe connecting a high-pressure reservoir at temperature T_1 , pressure P_1 , and chemical potential μ_1 to a pool of liquid that is held by surface tension to the glass surface at the low-pressure exit. The pressure in the exit region is effectively zero, so the fluid pool evaporates and its temperature drops to a lower temperature T_2 at which the evaporative heat flux Q_{evap} is balanced by thermal conduction from the glass. Fluid is blue and glass is gray.

temperature T_2 ,

$$J_{\text{evap}} = [P_{\text{SVP}}(T_2) - P_{\text{gas}}] \sqrt{\frac{m}{2\pi k T_2}}, \quad (3)$$

where P_{SVP} is the saturated vapor pressure of the liquid, $P_{\text{gas}} \approx 0$ is the pressure of the surrounding gas, m is the mass of a helium atom, and k is Boltzmann's constant. The RGA detector measures the total helium evaporating per unit time \dot{m}_{evap} ,

$$\dot{m}_{\text{evap}} = A_p J_{\text{evap}}, \quad (4)$$

where A_p is the surface area of the evaporating helium pool. In steady state, the temperature and size of the pool self-adjust so that the mass flow out of the pipe is the same as the evaporated flux. Determining T_2 and A_p requires a careful consideration of the heat and mass flows in our system.

We begin with the simplifying assumption that the normal fluid flow in the nanopipe is negligible and that all of the flow in the pipe is due to superfluid; a comparison of Figs. 2 and 3 shows that at the pressure drops corresponding to the flow discontinuity, the normal flow is never more than 5% of the total. The equation of motion for the superfluid velocity v_s is given by

$$\frac{\partial v_s}{\partial t} + \nabla \left(\frac{1}{2} v_s^2 + \mu \right) = 0, \quad (5)$$

where μ is the chemical potential. For steady-state one-dimensional flow in a pipe connecting fluid reservoirs at temperatures T_1 and T_2 and pressures P_1 and P_2 , the velocity is

$$v_s = \sqrt{2[\mu_1(T_1, P_1) - \mu_2(T_2, P_2)]}, \quad (6)$$

where we assume that $\mu_1 > \mu_2$ and the v_s is directed out of the reservoir and into the vacuum. When the inequality is reversed with $\mu_2 > \mu_1$, the superfluid will flow from the pool at the exit back into the reservoir. The chemical potential of the fluid can be computed for any T and P by integrating the thermodynamic relation $d\mu = -s dT + \frac{1}{\rho} dP$, where s is the entropy per unit mass and ρ is the density; both of these physical properties are available from standard tables [35–37].

For temperatures above 1 K, the entropic term in the equation dominates and since $s > 0$, the chemical potential is a monotonically decreasing function of temperature. This implies that for sufficiently small pressure drop, the chemical potential at the warm end of the pipe would be lower than at the cold end, so the superflow would flow into the reservoir. A critical finite pressure drop is

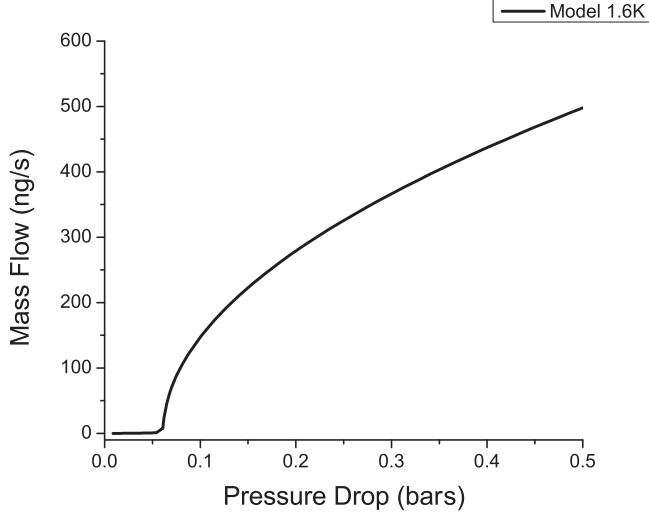


FIG. 6. Calculated pressure drop dependence of mass flow using Eqs. (6)–(8) for a $r = 131 \text{ nm} \times 30 \text{ mm}$ long glass pipe with $T_1 = 1.6 \text{ K}$.

required to establish a chemical potential gradient that drives the flow out of the reservoir and into the vacuum region of the apparatus.

The critical pressure drop required to overcome the $\Delta\mu$ caused by evaporative cooling can be calculated if the pool temperature T_2 is known. The steady-state heat balance of the pool is

$$L_v A_p [P_{\text{SVP}}(T_2) - P_{\text{gas}}] \sqrt{\frac{m}{2\pi k T_2}} = \frac{\Delta T}{R_K} A_p, \quad (7)$$

where L_v is the latent heat of evaporation, $\Delta T = (T_1 - T_2)$, and R_K is the Kapitza resistance between glass and ^4He , where we have used $R_K = 17.5 T^{3.6} \text{ (cm}^2 \text{ K)/W}$ as reported in Ref. [40]. The left-hand side of Eq. (7) is the heat flow due to evaporation and the right-hand side is the heat conducted across the solid-liquid interface. Assuming that the solid substrate is at temperature T_1 , Eq. (7) can be solved for the pool temperature T_2 . The values obtained for T_2 depend only weakly on T_1 and range from 0.7 to 0.8 K in our system. Once T_2 is determined, the critical reservoir pressure P_{cr} required to drive superflow out of the reservoir is given by the solution to

$$\mu_1(T_1, P_{cr}) = \mu_2(T_2, P_{\text{SVP}}(T_2)). \quad (8)$$

The surface area of the pool A_p is determined by the balance between the mass flow rate through the pipe and the evaporation rate of the pool:

$$A_p J_{\text{evap}} = \rho \pi r^2 \sqrt{2[\mu(T_1, P_1) - \mu(T_2, P_{\text{SVP}}(T_2))]} \quad (9)$$

For a given reservoir temperature T_1 , pressure $P_1 > P_{cr}$, and pool temperature T_2 , Eq. (9) can be solved for the pool radius r_p , which rises from zero at $P = P_{cr}$ to values in the range of 100 μm for reservoir pressures near 1 bar. Above the threshold pressure drop P_{cr} , this simplified model predicts a superfluid flow velocity that scales as $v_s \sim \sqrt{\mu_1} \sim \sqrt{P_1 - P_{cr}}$ and rises monotonically as shown in Fig. 6.

The only characteristic feature in the simplified model described above is the onset pressure P_{cr} , which we believe is related to the critical pressure P_c , which marks the start of the transition to much higher flow rates observed in data such as those shown in Fig. 3. A quantitative comparison between the data and the evaporation model requires a robust method of identifying P_c . This is complicated by the fact that in our experimental system, the transition occurs between a low-flow state and a

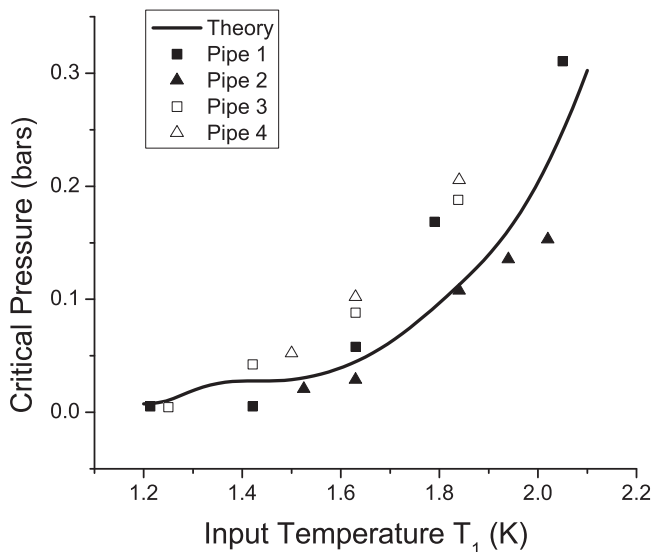


FIG. 7. Critical pressure as a function of the reservoir temperature T_1 . The solid curve is P_{cr} calculated from Eq. (8) vs T_1 . Data points mark the beginning of the steep rise in flow rate from data such as those in Fig. 4 using the Feynman critical velocity criterion described in the text.

high-flow state (rather than zero flow to finite flow described in the simplified model). To take this finite-flow rate at low-pressure drop into account, we identify P_c as the pressure drop at which the observed flow rate becomes equal to $\rho A v_F$, where A is the cross-sectional area of the pipe, ρ is the liquid helium density, and v_F is the well known Feynman critical velocity

$$v_F = \frac{\hbar}{2mR} \ln\left(\frac{2R}{a_0}\right), \quad (10)$$

where a_0 is the vortex core radius (in nm), which diverges as T approaches T_λ in the following way [41]:

$$a_0 \approx \frac{0.32}{(T_\lambda - T)^{1/2}}.$$

A comparison of experimental values of P_c determined using this criterion and the value of P_{cr} obtained using the evaporation model is shown in Fig. 7. The figure shows data from the entire range of pipe lengths and diameters; although there is some scatter, the model captures the trend in the data very well. Other operational definitions of P_c such as the point of maximum curvature at the foot of the rise in flow rate yield qualitatively similar results.

Although the model predicts P_c well, it does not explain the flow states above and below P_c . In particular, the simplified model predicts no flow for $P < P_c$, but a substantial flow much larger than the normal state flow is observed. For large pressure drops, the model predicts a mass flow that monotonically increases with pressure drop, but experiments show flow rates that are independent and even decrease with increasing pressure drop. These effects are discussed further below.

C. Low-pressure regime

If the pool at the low-pressure end of the pipe is at a lower temperature than the reservoir, a finite pressure drop will be required to establish a chemical potential gradient in the direction that drives superflow from the reservoir to the exit pool. For pressure drops below P_c , the simplified model suggest that superflow would tend to drain the superfluid in the pool back into the pipe and the

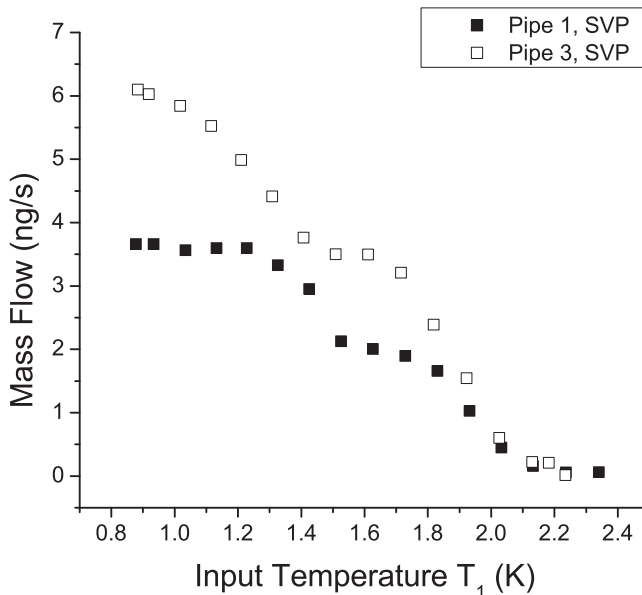


FIG. 8. Mass flow through pipes 1 (closed squares) and 3 (open squares), with radii $r = 131$ and 230 nm, respectively, as a function of the reservoir temperature T_1 . The pressure in the reservoir is the saturated vapor pressure $P_{\text{sat}}(T_1)$, which is always below P_c .

reservoir. In contrast, experiment shows a temperature-dependent flow from the reservoir into the vacuum that is over an order of magnitude higher than what can be accounted for by normal flow. Figure 8 shows the temperature dependence of the mass flow through pipes 1 and 3, with $r = 131$ and 230 nm, respectively, where the driving pressure drop is the saturated vapor pressure, which is always below P_c .

Both the magnitude and the strong temperature dependence of the mass flow below T_λ indicate that superfluidity is involved. Superfluid flows are often characterized by a critical velocity above which the flow becomes dissipative. The mass flow data of Fig. 8 can be converted into an average superfluid velocity v_s in the pipe using

$$v_s = \frac{\dot{m} - \dot{m}_n}{\rho_s(T_1)\pi r^2}, \quad (11)$$

where \dot{m} is the observed mass flow, \dot{m}_n is the normal mass flow, taken to be the mass flow just above T_λ multiplied by the normal fluid fraction, and $\rho_s(T_1)$ is the superfluid density at the saturated vapor pressure corresponding to the temperature of the reservoir T_1 . The normal fluid fraction and superfluid density were obtained from the same thermodynamic tables used earlier [35–37].

The superfluid velocity determined from Eq. (11) is compared to the Feynman critical velocity in Fig. 9. At low temperatures, v_F defined by Eq. (10) becomes independent of temperature and inversely proportional to the pipe radius, and the experimental data are consistent with both of these trends. Both the observed superfluid velocity v_s and v_F are strongly temperature dependent near T_λ . A similar temperature dependence has been seen previously [9,25,42]. There is a peculiar unexplained dip in the data at temperatures near 1.5 K that appeared in all the pipes we investigated.

The Feynman critical velocity is the velocity at which the Magnus force on a pinned vortex line that spans the pipe diameter will bend the vortex to cause pinch-off and continuous generation of vorticity [43]. Because of this instability, v_F is a natural velocity scale for superfluid flows and it is perhaps not surprising that our observed velocities at low-pressure drop are close to v_F . More paradoxical is the fact that there is any flow at all, since the simplified model of Eq. (6) implies that

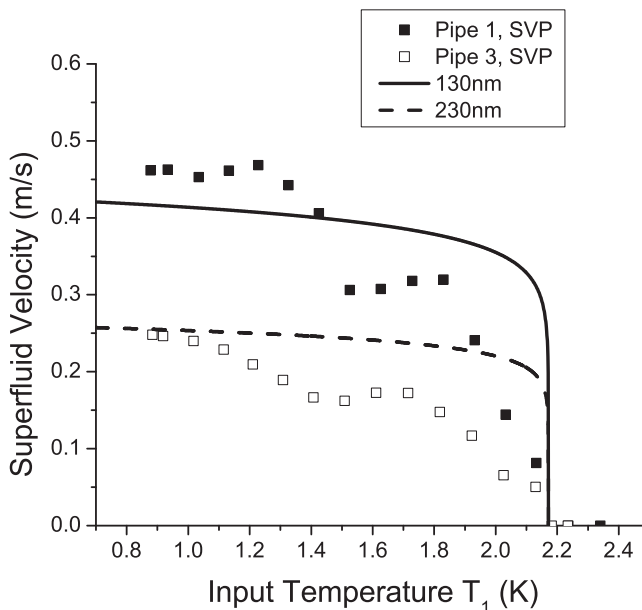


FIG. 9. Superfluid velocity through pipe 1, with $r = 131$ nm (closed squares), and pipe 3, with $r = 230$ nm (open squares), as a function of input temperature with the reservoir at SVP, which is less than P_c . The Feynman critical velocity from Eq. (10) for $R = 131$ nm (solid line) and $R = 230$ nm (dashed line) is also shown.

for $P < P_c$, the chemical potential gradient points in the wrong direction. One possible explanation for superflow into the vacuum even at small pressure drops is to invoke a more complex heat transfer model than described by Eq. (7). An implicit assumption in the simplified heat transfer model is that the temperature of the fluid in the pipe is the temperature of the reservoir T_1 throughout its length and that the temperature drops abruptly at the exit. The actual situation is certainly more complicated but difficult to model exactly. When the pool area is small, it is plausible that even small residual heat flows from the pipe will raise the temperature of the pool so that smaller pressure drops are sufficient to drive superflow into the vacuum against the thermal gradient.

D. High-pressure regime

The mass flow rate data for pressure drops above P_c are shown in Fig. 10. The mass flow of normal helium (2.3 K), which increases approximately linearly with pressure drop, is shown for pipe 1 as a benchmark. For low temperatures (1.2 K), where the superfluid fraction is nearly 1, the mass flow of superfluid is approximately independent of pressure drop up to pressures at which the bulk helium solidifies above 25.3 bars. The solidification of the bulk helium could be observed by a dramatic shift in the frequency of a quartz tuning fork that was submerged in the bulk helium. This pressure drop independent flow at low temperatures is illustrated again in Fig. 12, where mass flow rates for $\Delta P = 1.26$ and 23.3 bars appear to converge to the same value below 1.4 K.

For higher temperatures, the superfluid transition temperature depends on pressure: T_λ decreases linearly with pressure, ranging from 2.172 K at SVP to approximately 1.78 K at 30.4 bars. Because there is a pressure gradient in the nanopipe, this implies that the high-pressure end could be normal while the low-pressure end could be superfluid, i.e., the superfluid transition could occur inside the pipe. At intermediate temperatures (1.8 K) the flow rate actually decreases with increasing pressure drop. This is likely due to $\Delta T = T_\lambda - T_1$ decreasing with increasing pressure, thus decreasing the superfluid fraction. Furthermore, although we have varied the nanopipe length by over an order of magnitude, the length appears to have little to no effect on the superfluid mass flow.

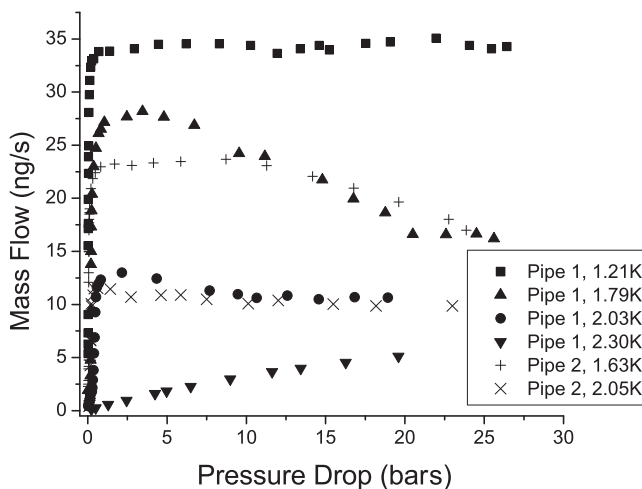


FIG. 10. Mass flow as a function of pressure drop through pipes 1 and 2 for a range of temperatures of the high-pressure reservoir T_1 : pipe 1 for 1.21 K (■), 1.79 K (▲), and 2.03 K (●) and pipe 2 for 1.63 K (+) and 2.05 K (×). Normal state flow through a 2-mm nanopipe at 2.30 K (▼) is shown for comparison. Here $P_c < 1$ bar, so most of the data are in the high-pressure regime. Note that the length of the nanopipe has very little effect on the mass flow.

At pressure drops above P_c , the temperature dependence of the superfluid velocity v_s is drastically different than at low pressure. Figure 9 shows the temperature dependence of v_s at low pressures compared to the Feynman critical velocity (10) for pipes of $r = 131$ and 230 nm. For $P < P_c$, the superfluid velocity decreases with increasing temperature. In Fig. 11, we perform the same analysis for pressure drops above P_c , but for this case the velocity is largely temperature independent, even increasing slightly with increasing temperature before dropping sharply, very close to T_λ . This behavior is in sharp contrast to the power-law behavior observed in the smaller pores of Ref. [25]. Although v_s is roughly proportional to $1/R$ as in the Feynman formula, the low-temperature values of v_s are much higher than the values observed for $P < P_c$, and to get even approximate agreement with the data, the predictions of Eq. (10) need to be multiplied by a factor of 11. A comparison of the flow rates through nanopipes of length 2 and 30 mm shows that for a given pressure drop, the flow is essentially independent of the nanopipe length.

The schematic diagram of Fig. 5 implies that there are temperature and pressure gradients in the nanopipe. Although our data do not directly address the spatial dependence of the gradients, they do provide some qualitative insight. For a relatively-low-pressure drop where the pressure drop dependence of the superfluid transition temperature is negligible, our observations are consistent with the assumption that the temperature in the nanopipe is the same as in the high-pressure reservoir and the temperature gradients are confined to a short region near the exit. For example, the flow data shown in Fig. 11 shows no sign of superflow for input reservoir temperatures above 2.17 K, even though the temperature of the fluid pool on the low-pressure end is certainly below T_λ . Similarly, for the nominally normal state flow shown in Fig. 2 there must be a superfluid-normal boundary somewhere in the nanopipe, but apparently it is near the end because the standard viscous flow equations using the nominal geometry explain the data. At high pressures, the superfluid transition temperature can be significantly depressed. Figure 12 compares temperature dependence of flow rates at high and low driving pressures. For $P = 23.3$ bars, the superfluid transition is at $T = 1.82$ K, so naively one would not expect superflow for reservoir temperatures above this value. The data nevertheless show a small increase in flow rate at T_λ , but also a more significant but broader increase as the temperature drops below 1.82 K. This behavior suggests that the combination of temperature and pressure gradients can affect the location of the supernormal boundary in the nanopipe.

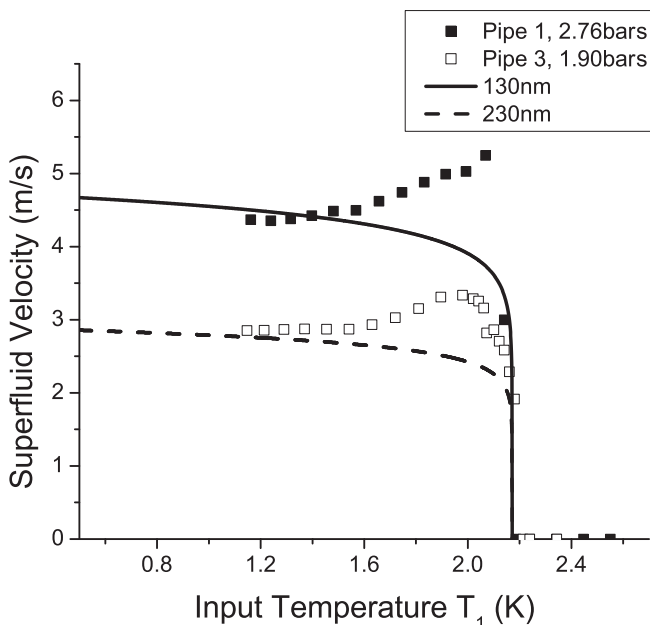


FIG. 11. Superfluid velocity through pipe 1, with $r = 131$ nm (closed squares), and pipe 3, with $r = 230$ nm (open squares), for a constant pressure drop above P_c as a function of temperature. The curves show the Feynman critical velocity for $R = 131$ nm (solid line) and $R = 230$ nm (dashed line) multiplied by a constant factor $\alpha = 11$.

An ideal dissipationless superfluid cannot sustain steady-state flow in a pipe subject to a chemical potential gradient; some form of dissipation is required to balance the pressure work done on the fluid. Dissipation in a superfluid is intimately related to the formation and motion of vortex lines. The Anderson-Josephson relation

$$\Delta P = \frac{\rho \dot{N} h}{m} \quad (12)$$

relates the pressure drop to the rate \dot{N} that vortices must be created and cross the flow lines [44] to account for ΔP . For a 20.3-bar pressure drop across an $r = 131$ nm \times 2 mm long pipe, such as that shown in Fig. 11, the equation requires approximately 10^{11} vortices per second to cross the flow path. If the pressure gradient is approximately constant and the vortex velocity transverse to the flow is approximately the same as the axial flow velocity in the pipe, the number density of vortices $n \sim 10^{20}$ m $^{-3}$ and the mean spacing between vortices is ~ 220 nm.

The vortices can be produced either by thermal nucleation or by a “mill” process that amplifies preexisting pinned vortices [45]. The fact that the flow rate becomes essentially independent of temperature at low temperature rules out thermal nucleation. For a pinned vortex to bow out across the diameter of the pipe requires a time of order the pipe radius divided by the flow velocity, which for our pipes is approximately 10^{-7} s. This implies that for our pipes, at least 10^4 pinned vortices would be needed to generate the measured pressure drop. Schwarz has pointed out that pinned vortices in a finite pipe will be advected downstream and flushed out of the pipe, so they need to be continuously generated [20,45]. One proposal to accomplish this is to have several vortices with pinning sites outside the inlet. The other pinning sites can propagate down the tube in a helical wave that will interact and generate a vortex tangle if the velocity is above a critical velocity estimated to be $20\kappa/R$, where κ is the quantum of circulation. For our pipes, this critical velocity is approximately 30 m/s, which is about an order of magnitude higher than the flow velocities we observe.

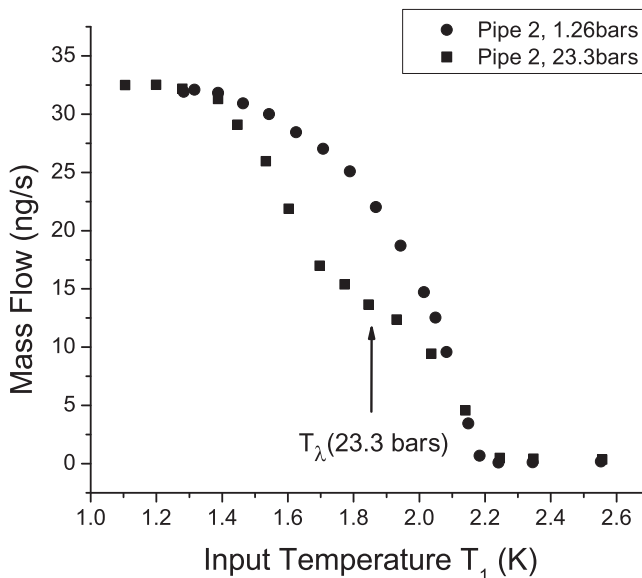


FIG. 12. Mass flow through pipe 2 ($r = 132 \text{ nm} \times 30 \text{ mm}$) as a function of the temperature T_1 of the high-pressure reservoir for two values of the pressure in the high-pressure reservoir. For $P_1 = 1.26 \text{ bars}$ (closed circles), the superfluid transition temperature is 2.17 K and the mass flow increases smoothly as the reservoir temperature is lowered below that value. For $P_1 = 23.3 \text{ bars}$ (closed squares) the superfluid transition temperature is 1.82 K. As the temperature is lowered below 2.17 K, the flow increases abruptly even though the fluid in the high-pressure reservoir is normal (the fluid pool at the low-pressure outlet is superfluid, however). As the reservoir is cooled further below its superfluid transition, there is another steplike feature in the flow rate, which may be due to motion of the superfluid-normal boundary in the nanopipe.

IV. CONCLUSION

The behavior of superfluid helium flow through single nanopipes into a vacuum was studied for inlet pressures ranging from 0 to 30 bars. Surface tension effects require the superfluid exiting the nanopipe on the vacuum side to form a pool that subsequently evaporates at a rate determined by heat transfer from the substrate. The temperature of the pool typically reaches values near 0.7 K and is only weakly dependent on the temperature of the high-pressure reservoir. The fact that flow through the nanopipe connects two liquid reservoirs at different temperatures has important implications for the analysis of this type of experiment. Superfluid flow is driven by changes in chemical potential that are generated by temperature and pressure gradients. Superfluid will flow toward regions of high temperature and low pressure, but these two gradients are opposed to each other for most operating parameters of our apparatus. We have observed a transition in flow regimes at a critical pressure drop, which appears to be the pressure gradient required to generate a net chemical potential gradient directed toward the low-pressure end of the nanopipe. The flow transition at P_c was observed in all of our pipes. It does not seem to occur in more conventional flow experiments [9,10,46–48] and was not observed in previous experiments on flow into a vacuum through smaller pores [23,25].

For pressure drops below the critical pressure drop P_c , our simplified model suggests that the flow would be directed toward the high-pressure side of the nanopipe, which would drain the fluid pool at the exit and result in no net flow. In contrast, our measurements with $P < P_c$ show a strongly-temperature-dependent superfluid flow into the low-pressure side of the apparatus. This discrepancy may be due to an oversimplification of the heat transfer model or to the onset of a more complex time varying or spatially inhomogeneous flow. Nevertheless, increasing the driving pressure beyond P_c where the chemical potential gradient changes sign results in an abrupt increase in the

mass flow rate by roughly an order of magnitude. Above P_c the superfluid velocity is essentially independent of temperature and of the length of the nanopipe. For low temperatures and temperatures near T_λ , the mass flow is also independent of the pressure drop. At intermediate temperatures, the mass flow actually decreases with increasing pressure drop, which may be related to motion of the supernormal-normal interface inside the nanopipe and the decrease in the superfluid fraction with increasing pressure. Mass flow rates that are independent of pressure drop have been seen in previous experiments on superfluid flow connecting two nominally isothermal liquid reservoirs with pressure drops of only a few μbars [46]; a remarkable feature of our data is that the pressure drop independence of the mass flow extends all the way to the solidification pressure. In a future study we hope to apply the Biot-Savart vortex tangle model [45,49] and the detailed two fluid hydrodynamic models [19,50] to produce a quantitative comparison with our experimental data.

ACKNOWLEDGMENT

We thank Angel Velasco for help with the early versions of the apparatus and the W. M. Keck Foundation for financial support.

-
- [1] P. W. Anderson, Considerations on the flow of superfluid helium, *Rev. Mod. Phys.* **38**, 298 (1966).
 - [2] J. S. Langer and M. E. Fisher, Intrinsic Critical Velocity of a Superfluid, *Phys. Rev. Lett.* **19**, 560 (1967).
 - [3] E. Varoquaux, Anderson's considerations on the flow of superfluid helium: Some offshoots, *Rev. Mod. Phys.* **87**, 803 (2015).
 - [4] H. A. Notarys, Pressure-Driven Superfluid Helium Flow, *Phys. Rev. Lett.* **22**, 1240 (1969).
 - [5] G. G. Ihas, O. Avenel, R. Aarts, R. Salmelin, and E. Varoquaux, Quantum Nucleation of Vortices in the Flow of Superfluid ^4He Through an Orifice, *Phys. Rev. Lett.* **69**, 327 (1992).
 - [6] W. De Haas, A. Hartoog, H. Van Beelen, R. de Bruyn Ouboter, and K. W. Taconis, Dissipation and oscillations in the flow of the saturated He II film, *Physica* **75**, 311 (1974).
 - [7] G. Marees, R. P. Slegtenhorst, and H. Vanbeelen, Measurements of the isothermal flow of helium II in narrow tubes, *J. Low Temp. Phys.* **51**, 165 (1983).
 - [8] T. Satoh and M. Okuyama, Adiabatic flow of He II: IV. Superfluid frictional force F_s , *Physica B* **172**, 420 (1991).
 - [9] G. B. Hess, Critical Velocities in Superfluid Helium Flow Through 10- μm -Diameter Pinholes, *Phys. Rev. Lett.* **27**, 977 (1971).
 - [10] J. P. Hulin, D. D'Humieres, B. Perrin, and A. Libchaber, Critical velocities for superfluid-helium flow through a small hole, *Phys. Rev. A* **9**, 885 (1974).
 - [11] M. E. Banton, Gravitational flow of superfluid-helium through small orifices, *J. Low Temp. Phys.* **16**, 211 (1974).
 - [12] O. Avenel and E. Varoquaux, Observation of Singly Quantized Dissipation Events Obeying the Josephson Frequency Relation in the Critical Flow of Superfluid ^4He Through an Aperture, *Phys. Rev. Lett.* **55**, 2704 (1985).
 - [13] Y. Sato and R. E. Packard, Superfluid helium quantum interference devices: Physics and applications, *Rep. Prog. Phys.* **75**, 016401 (2012).
 - [14] J. S. Brooks, B. B. Sabo, P. C. Schubert, and W. Zimmermann, Jr., Helmholtz-resonator measurements of the superfluid density of liquid ^4He in submicrometer-diameter channels, *Phys. Rev. B* **19**, 4524 (1979).
 - [15] J. Steinhauer, K. Schwab, Y. Mukharsky, J. C. Davis, and R. E. Packard, The determination of the energy barrier for phase slips in superfluid ^4He , *J. Low Temp. Phys.* **100**, 281 (1995).
 - [16] G. Kukich, R. P. Henkel, and J. D. Reppy, Decay of Superfluid "Persistent Currents", *Phys. Rev. Lett.* **21**, 197 (1968).

- [17] G. L. Mills, A. J. Mord, and H. A. Snyder, Pressure maxima in the flow of superfluid ^4He in tubes, *Phys. Rev. B* **49**, 666 (1994).
- [18] A. J. Mord, H. A. Snyder, and D. A. Newell, End-to-end modelling of He II flow systems, *Cryogenics* **32**, 291 (1992).
- [19] K. Takamatsu, N. Fujimoto, Y. F. Rao, and K. Fukuda, Numerical study of flow and heat transfer of superfluid helium in capillary channels, *Cryogenics* **37**, 829 (1997).
- [20] K. W. Schwarz, Three-dimensional vortex dynamics in superfluid ^4He : Line-line and line-boundary interactions, *Phys. Rev. B* **31**, 5782 (1985).
- [21] K. W. Schwarz, Numerical experiments on single quantized vortices, *Physica B* **197**, 324 (1994).
- [22] M. Tsubota, M. Kobayashi, and H. Takeuchi, Quantum hydrodynamics, *Phys. Rep.* **522**, 191 (2013).
- [23] M. Savard, G. Dauphinais, and G. Gervais, Hydrodynamics of Superfluid Helium in a Single Nanohole, *Phys. Rev. Lett.* **107**, 254501 (2011).
- [24] A. E. Velasco, C. Yang, Z. S. Siwy, M. E. Toimil-Molares, and P. Taborek, Flow and evaporation in single micrometer and nanometer scale pipes, *Appl. Phys. Lett.* **105**, 033101 (2014).
- [25] P.-F. Duc, M. Savard, M. Petrescu, B. Rosenow, A. Del Maestro, and G. Gervais, Critical flow and dissipation in a quasi-one-dimensional superfluid, *Sci. Adv.* **1**, 1 (2015).
- [26] J. C. Burton, E. Van Cleve, and P. Taborek, A continuous ^3He cryostat with pulse-tube pre-cooling and optical access, *Cryogenics* **51**, 209 (2011).
- [27] A. Demann, S. Mueller, and S. B. Field, 1 K cryostat with sub-millikelvin stability based on a pulse-tube cryocooler, *Cryogenics* **73**, 60 (2016).
- [28] P. Kittel, Liquid helium pumps for in-orbit transfer, *Cryogenics* **27**, 81 (1987).
- [29] H. Nakai, N. Kimura, M. Murakami, T. Haruyama, and A. Yamamoto, Superfluid helium flow through porous media, *Cryogenics* **36**, 667 (1996).
- [30] A. E. Velasco, S. G. Friedman, M. Pevarnik, Z. S. Siwy, and P. Taborek, Pressure-driven flow through a single nanopore, *Phys. Rev. E* **86**, 025302(R) (2012).
- [31] See Supplemental Material at <http://link.aps.org/supplemental/10.1103/PhysRevFluids.1.054102> for an SEM image of the pipe entrance.
- [32] R. Blaauwgeers, M. Blazkova, M. Clovecko, V. B. Eltsov, R. de Graaf, J. Hosio, M. Krusius, D. Schmoranzler, W. Schoepe, L. Skrbek, P. Skyba, R. E. Solntsev, and D. E. Zmeev, Quartz tuning fork: Thermometer, pressure- and viscometer for helium liquids, *J. Low Temp. Phys.* **146**, 537 (2007).
- [33] D. O. Clubb, O. V L Buu, R. M. Bowley, R. Nyman, and J. R. Owers-Bradley, Quartz tuning fork viscometers for helium liquids, *J. Low Temp. Phys.* **136**, 1 (2004).
- [34] F. M. Huisman, A. E. Velasco, E. Van Cleve, and P. Taborek, Quartz tuning forks as cryogenic vacuum gauges, *J. Low Temp. Phys.* **177**, 226 (2014).
- [35] J. S. Brooks and R. J. Donnelly, The calculated thermodynamic properties of superfluid helium-4, *J. Phys. Chem. Ref. Data* **6**, 51 (1977).
- [36] J. M. Goodwin, The viscosity of pressurized ^4He above T_λ , *Physica* **76**, 177 (1974).
- [37] R. J. Donnelly and C. F. Barenghi, The observed properties of liquid helium at the saturated vapor pressure, *J. Phys. Chem. Ref. Data* **27**, 1217 (1998).
- [38] R. E. Grisenti and J. P. Toennies, Cryogenic Microjet Source for Orthotropic Beams of Ultralarge Superfluid Helium Droplets, *Phys. Rev. Lett.* **90**, 234501 (2003).
- [39] W. van Hoeve, S. Gekle, J. H. Snoeijer, M. Versluis, M. P. Brenner, and D. Lohse, Breakup of diminutive Rayleigh jets, *Phys. Fluids* **22**, 122003 (2010).
- [40] G. L. Pollack, Kapitza resistance, *Rev. Mod. Phys.* **41**, 48 (1969).
- [41] C. F. Barenghi, R. J. Donnelly, and W. F. Vinen, Friction on quantized vortices in helium II. A review, *J. Low Temp. Phys.* **52**, 189 (1983).
- [42] W. Zimmermann, C. A. Lindensmith, and J. A. Flaten, The interpretation of phase-slip and critical-velocity data from the flow of superfluid He-4 through a $2\ \mu\text{m}$ by $2\ \mu\text{m}$ aperture, *J. Low Temp. Phys.* **110**, 497 (1998).
- [43] R. J. Donnelly, *Quantized Vortices in Helium II*, 2nd ed. (Cambridge University Press, Cambridge, 1991).
- [44] R. E. Packard, The role of the Josephson-Anderson equation in superfluid helium, *Rev. Mod. Phys.* **70**, 641 (1998).

- [45] K. W. Schwarz, Phase Slip and Turbulence in Superfluid ^4He : A Vortex Mill that Works, [Phys. Rev. Lett.](#) **64**, 1130 (1990).
- [46] G. M. Shifflett and G. B. Hess, Intrinsic critical velocities in superfluid He-4 flow-through 12- μm diameter orifices near T_λ : Experiments on the effect of geometry, [J. Low Temp. Phys.](#) **98**, 591 (1995).
- [47] E. Varoquaux, M. W. Meisel, and O. Avenel, Onset of the Critical Velocity Regime in Superfluid ^4He at Low-Temperature, [Phys. Rev. Lett.](#) **57**, 2291 (1986).
- [48] A. Talmi and J. Landau, Isothermal flow of superfluid helium through narrow channels, [J. Low Temp. Phys.](#) **12**, 275 (1973).
- [49] M. Tsubota and H. Adachi, Simulation of counterflow turbulence by vortex filaments, [J. Low Temp. Phys.](#) **162**, 367 (2011).
- [50] H. A. Snyder and A. J. Mord, Calculation of He II flow in tubes, [J. Low Temp. Phys.](#) **86**, 177 (1992).